

Observation of spinful square-root and higher-order topological phases enriched by synthetic spin-orbit coupling

Yang Kou(寇杨), Yi Li(李一), Jia-Hui Zhang(张佳辉), Liantuan Xiao(肖连团), Suotang Jia(贾锁堂), Feng Mei(梅锋)

Citation: Chin. Phys. B. 35, 097103 (2026). DOI: 10.1088/1674-1056/ae4b2c |
CSTR: 32038.14.CPB.ae4b2c
http://cpb.iphy.ac.cn; http://iopscience.iop.org/cpb

What follows is a list of articles you may be interested in

ARPES study of Y2O2Bi single crystals: Intrinsic electronic structure of Bi square nets

Yun-Bo Wu(吴云波), Tong-Rui Li(李彤瑞), Zhi-Peng Cao(曹志鹏), Zhan-Feng Liu(刘站锋), Yu-Liang Li(李昱良), Zheng-Ming Shang(尚政明), Xin Zheng(郑新), Hui Tian(田慧), Zong-Yi Wang(王宗一), Yu-Tong Bi(毕雨桐), Hao-Yang Zhou(周浩洋), Yi Liu(刘毅), Guo-Bin Zhang(张国斌), Zheng-Tai Liu(刘正太), Da-Wei Shen(沈大伟), Li-Dong Zhang(张李东), Sheng-Tao Cui(崔胜涛), Zhe Sun(孙喆)
Chin. Phys. B. 35, 047101 (2026). DOI: 10.1088/1674-1056/ae04d9 | CSTR: 32038.14.CPB.ae04d9

Enhancement of spin-orbit torque efficiency by tailoring interfacial spin-orbit coupling in Pt-based magnetic multilayers

Wenqiang Wang(王文强), Gengkuan Zhu(朱耿宽), Kaiyuan Zhou(周恺元), Xiang Zhan(战翔), Zui Tao(陶醉), Qingwei Fu(付清为), Like Liang(梁力克), Zishuang Li(李子爽), Lina Chen(陈丽娜), Chunjie Yan(晏春杰), Haotian Li(李浩天), Tiejun Zhou(周铁军), Ronghua Liu(刘荣华)
Chin. Phys. B. 31, 097504 (2022). DOI: 10.1088/1674-1056/ac76aa

Influence of Rashba spin-orbit coupling on Josephson effect in triplet superconductor/two-dimensional semiconductor/triplet superconductor junctions

Bin-Hao Du(杜彬豪), Man-Ni Chen(陈嫚妮), Liang-Bin Hu(胡梁宾)
Chin. Phys. B. 31, 077201 (2022). DOI: 10.1088/1674-1056/ac587e

---

Observation of spinful square-root and higher-order topological phases enriched by synthetic spin–orbit coupling

Yang Kou(寇杨)[1], Yi Li(李一)[1], Jia-Hui Zhang(张佳辉)[1], Liantuan Xiao(肖连团)[1,2], Suotang Jia(贾锁堂)[1,2], and Feng Mei(梅锋)[1,2,†]

[1] *State Key Laboratory of Quantum Optics Technologies and Devices, Institute of Laser Spectroscopy, Shanxi University, Taiyuan* 030006, *China*
[2] *Collaborative Innovation Center of Extreme Optics, Shanxi University, Taiyuan* 030006, *China*

(Received 9 January 2026; revised manuscript received 11 February 2026; accepted manuscript online 27 February 2026)

Topological phases induced by spin–orbit coupling (SOC) have been widely investigated and realized in various artificial systems. In this work, we theoretically propose and experimentally demonstrate two distinct spinful topological phases enriched by one- and two-dimensional SOC using topological circuit metamaterials. First, we report the emergence of a spinful square-root topological phase in a one-dimensional SOC-induced Aharonov–Bohm (AB) caging lattice model, characterized by spin-dependent topological winding numbers. Second, we present a spinful higher-order topological phase in a two-dimensional dimerized SOC lattice model, which hosts eight topological corner modes and is characterized by multipole chiral numbers. Experimentally, we synthesize effective spin–orbit couplings in a circuit metamaterial and implement both lattice models, with impedance measurements directly revealing their characteristic topological boundary and corner responses. Our work provides new physical insights into SOC-induced and SOC-enriched synthetic topological phases.

Keywords: square-root topological phase, higher-order topological phase, synthetic spin–orbit coupling

PACS: 71.70.Ej, 64.70.Tg, 03.65.Vf

DOI: 10.1088/1674-1056/ae4b2c **CSTR:** 32038.14.CPB.ae4b2c

1. Introduction

Topological phases of matter are now of great interest across many areas of physics.[1–3] Distinct from conventional phases characterized by local order parameters, topological phases are protected by global topological invariants,[4,5] which endow them with intrinsic robustness against perturbations and noise. This robustness gives rise to a wealth of novel physical phenomena and underpins promising technological applications. Over the past decades, topological phases have been extensively investigated in a wide range of material and artificial platforms owing to their unconventional boundary states and transport properties, including photonic,[6–19] acoustic,[20–26] cold-atom,[27–29] and electrical-circuit platforms.[30–34] Importantly, these synthetic platforms offer exceptional flexibility in engineering lattice geometries, coupling strengths, and symmetries, thereby enabling systematic and controllable exploration of topological band theory beyond the intrinsic limitations of solid-state materials.

Spin–orbit coupling (SOC) describes an effective interaction that couples internal spin degrees of freedom to the motion or geometry of a system, and it plays a central role in the emergence of spinful topological phases. Realizing SOC in artificial platforms enables controlled access to spin–momentum coupling and effective spin-dependent gauge fields, which are difficult to isolate or tune in natural solid-state materials. Such synthetic SOC has been experimentally implemented in recent years in ultracold atoms,[35–45] photonic systems,[46] and electrical circuits[47] by engineering spin-dependent phases in the hopping or coupling processes. These implementations allow for the controlled engineering of spin-dependent band structures and coupling processes, providing a direct route to tailoring spin-resolved topological features. This mechanism gives rise to well-established topological phases, including time-reversal–invariant Z_2 topological insulators, Chern topological phases, and more generally symmetry-protected crystalline topological phases with spin-resolved boundary states.

In this work, we investigate two lattice models whose topological phases are induced and enriched by synthetic SOC. The first model is a one-dimensional (1D) SOC-induced Aharonov–Bohm (AB) caging lattice, in which the interplay between destructive interference and spin-dependent hopping leads to a spinful square-root topological phase. This phase is characterized by spin-resolved topological winding numbers and enriched boundary localization. The second model is a two-dimensional (2D) dimerized SOC lattice that realizes a spinful higher-order topological phase, hosting multiple robust corner modes. The multiplicity of these corner states reflects SOC-enriched higher-order topology and is captured by multipole chiral numbers. In both models, SOC does not merely realize known topological phases but fundamentally enriches their boundary physics, manifested by the dou-

†Corresponding author. E-mail: meifeng@sxu.edu.cn

© 2026 Chinese Physical Society and IOP Publishing Ltd. All rights, including for text and data mining, AI training, and similar technologies, are reserved.

bling and reorganization of the associated topological boundary states in a spin-dependent manner. We further implement both lattice models in circuit metamaterials and directly probe their SOC-induced and SOC-enriched topological responses through impedance spectroscopy and spatial voltage mapping.

2. Spinful square-root topological phase in a SOC AB caging lattice

2.1. SOC AB caging

We first consider a single-channel quantum wire with Rashba SOC oriented along an arbitrary direction $\hat{\gamma}$ in the x–y plane. The corresponding Hamiltonian is given by[48]

$$H = \frac{p_\gamma^2}{2m} - \frac{\hbar k_{\rm SO}}{m} p_\gamma (\boldsymbol{\sigma} \times \hat{z}) \cdot \hat{\gamma}, \tag{1}$$

where p_γ is the momentum operator along $\hat{\gamma}$, m is the effective electron mass, and $\boldsymbol{\sigma} = (\sigma_x, \sigma_y, \sigma_z)$ denotes the Pauli matrices. The parameter $k_{\rm SO}$ characterizes the Rashba SOC strength and is related to the spin–precession length by $L_{\rm SO} = \pi/k_{\rm SO}$. To construct the lattice model, we treat each bond as such a SOC quantum wire with uniform length L and identical $k_{\rm SO}$. The unit cell contains three lattice nodes labeled A, B, and C, as illustrated in Fig. 1(a). Consider an electron initially in an arbitrary spin state $|\sigma\rangle$ at site A: it can propagate to the next A site via two distinct paths, namely the upper path through B and the lower path through C. Along the upper path, the spin rotates sequentially about $\hat{z} \times \hat{\gamma}_1$ and then $\hat{z} \times \hat{\gamma}_2$, whereas along the lower path, the rotation order is reversed. The spin states at the target A site along these two paths are

$$|s_1\rangle = \hat{R}_{\hat{\gamma}_2} \hat{R}_{\hat{\gamma}_1} |\sigma\rangle, \quad |s_2\rangle = \hat{R}_{\hat{\gamma}_1} \hat{R}_{\hat{\gamma}_2} |\sigma\rangle, \tag{2}$$

where $|s_1\rangle$ and $|s_2\rangle$ denote the spin states along the upper and lower paths, respectively, and $\hat{R}_{\hat{\gamma}} = \exp[-{\rm i}(\boldsymbol{\sigma} \cdot (\hat{z} \times \hat{\gamma})) k_{\rm SO} L]$ is the spin-rotation operator induced by SOC along a bond in the $\hat{\gamma}$ direction, with rotation axis $\hat{z} \times \hat{\gamma}$. Destructive interference between the two paths occurs when the rotation operators anticommute, $\{\hat{R}_{\hat{\gamma}_1}, \hat{R}_{\hat{\gamma}_2}\} = 0$. In our setup, $\hat{\gamma}_1$ and $\hat{\gamma}_2$ are orthogonal ($\hat{\gamma}_1 \cdot \hat{\gamma}_2 = 0$), so this condition is satisfied when $k_{\rm SO} L = (n + 1/2)\pi$, with n chosen as an even integer. Under this condition, the rotation operators reduce to

$$\hat{R}_{\hat{\gamma}_1} = -{\rm i}\sigma_y, \quad \hat{R}_{\hat{\gamma}_2} = -{\rm i}\sigma_x. \tag{3}$$

The spin states along the two paths then satisfy $|s_1\rangle = -|s_2\rangle$, resulting in destructive interference that completely localizes the electron within the diamond chain. This mechanism is analogous to the Aharonov–Bohm (AB) cage effect,[49,50] where the phase difference between paths originates from the enclosed magnetic flux. In our system, however, the phase difference arises from the Rashba spin–orbit interaction.[51,52] Motivated by this analogy, we refer to the elementary square-loop structure in our system as a SOC AB cage.

2.2. Theoretical model

Building on the Rashba-induced localization mechanism, we construct a 1D SOC AB cage model based on the diamond-chain geometry shown in Fig. 1(a). The unit cell highlighted by the yellow dashed box in Fig. 1(a) contains three lattice sites (A, B, and C), each carrying two pseudospin degrees of freedom, and the inter-site couplings are implemented through the SOC σ_x and σ_y. Within the single-particle tight-binding approximation, the Hamiltonian in momentum space reads

$$H(k) = \begin{pmatrix} 0 & \sigma_x {\rm e}^{-{\rm i}k} + \sigma_y & \sigma_x + \sigma_y {\rm e}^{-{\rm i}k} \\ \sigma_x {\rm e}^{{\rm i}k} + \sigma_y & 0 & 0 \\ \sigma_x + \sigma_y {\rm e}^{{\rm i}k} & 0 & 0 \end{pmatrix}, \tag{4}$$

which yields three perfectly flat bands at $E(k) = 0, \pm 2$. Because the eigenstates are twofold degenerate, the usual 1D winding number is no longer applicable. To capture the topology in this setting, we instead use a non-Abelian topological invariant[53,54] that tracks the geometric evolution of the degenerate subspace across the Brillouin zone

$$\gamma = \int_0^{2\pi} {\rm Tr}(A)\, {\rm d}k, \tag{5}$$

where $A(k) * \alpha, \beta = {\rm i}\langle \psi * \alpha(k) | \partial_k | \psi_\beta(k) \rangle$ denotes the non-Abelian Berry connection, and α, β label the degenerate eigenstates. A nontrivial value of γ reflects a non-Abelian Berry phase accumulated during adiabatic evolution, revealing the geometric structure of the degenerate band manifold.[55] This non-Abelian character originates from the non-commuting SOC terms, which mix the spin subspaces and give rise to a matrix-valued Berry connection.

Having established the non-Abelian topological structure of the Bloch bands, we now turn to the real-space description. In real space, the tight-binding Hamiltonian is written as

$$H = \sum_n \left(\sigma_y a_n^\dagger b_n + \sigma_x a_n^\dagger c_n + \sigma_y a_n^\dagger c_{n-1} + \sigma_x a_n^\dagger b_{n-1} + {\rm h.c.} \right), \tag{6}$$

where $a_n^\dagger$ ($b_n^\dagger$, $c_n^\dagger$) and a_n (b_n, c_n) denote the creation and annihilation operators at the A (B, C) sites of the n-th unit cell. To investigate the SOC caging effect, we consider a 1D lattice with $N = 6$ unit cells under open boundary conditions (OBC). The energy spectrum in Fig. 1(b) features three perfectly flat bands at $E = 0$ and $E = \pm 2$, along with a pair of in-gap states at $E = \pm\sqrt{2}$ localized at the boundary. The flat bands indicate that the eigenstates at $E = 0, \pm 2$ are highly localized, a feature arising from destructive interference enforced by the non-Abelian gauge structure. The spatial density distributions in Fig. 1(c) reveal the nature of these states: the in-gap states at $E = \pm\sqrt{2}$ are confined to the left boundary, the $E = 0$ states form dark states with vanishing amplitude on all A sites, and the states at $E = \pm 2$ correspond to bulk modes, with density primarily concentrated on the A sites and their neighboring B and C sites. These spatial profiles clearly distinguish boundary, dark, and bulk states, illustrating the interference-induced localization characteristic of the SOC AB cage.

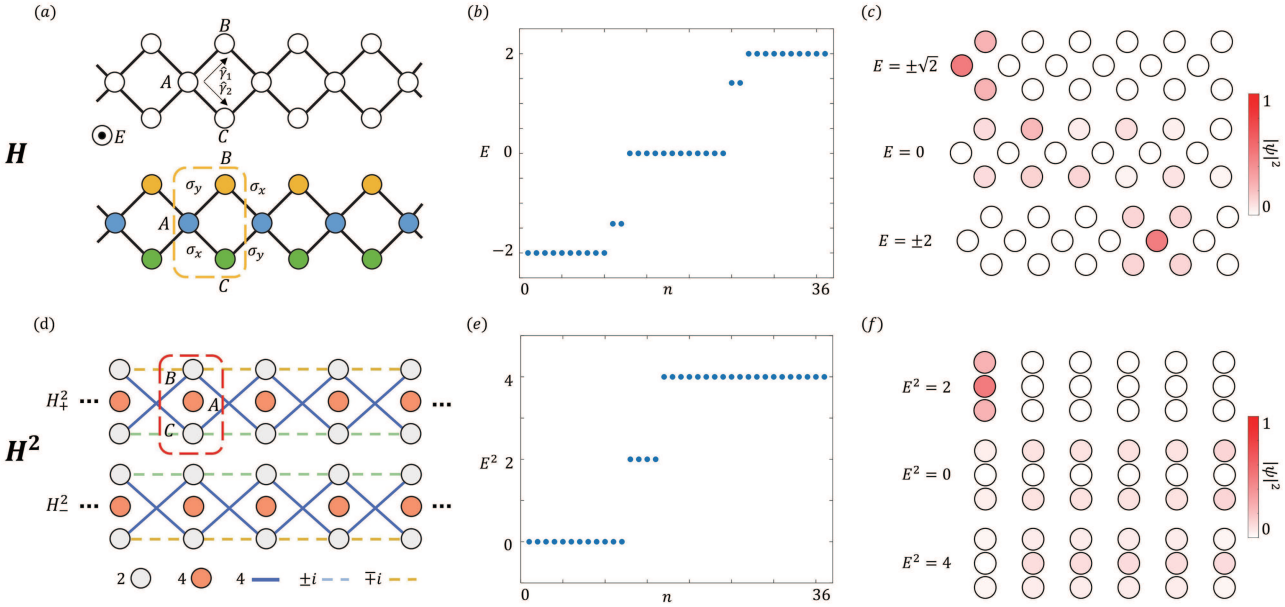


Fig. 1. (a) Schematic of the SOC-based diamond chain (top) and the corresponding 1D SOC AB cage model (bottom), consisting of three lattice sites A, B, and C (yellow dashed circle). The inter-site couplings act on the pseudospin degrees of freedom through σ_x and σ_y. (b) Energy spectrum for $N = 6$ unit cells under OBC, showing three flat bands at $E = 0, \pm 2$ and in-gap boundary states at $E = \pm\sqrt{2}$. (c) Spatial density distributions of representative eigenstates: $E = \pm\sqrt{2}$ (boundary states), $E = 0$ (dark states), and $E = \pm 2$ (bulk states). (d) Squared Hamiltonian H^2 shown as two decoupled lattices in the spin-up (top) and spin-down (bottom) subspaces, where each unit cell (red dashed box) contains an isolated site A and coupled sites B and C. (e,f) Same as (b,c), but for the squared Hamiltonian H^2. There are flat bands at $E = 0$ and $E = 4$ originating from the $E = 0$ and $E = \pm 2$ states of H, while the in-gap states at $E = 2$ are boundary-localized modes inherited from the $E = \pm\sqrt{2}$ states.

2.3. Square-root topological phase

Within the square-root topological framework, the squared Hamiltonian H^2 retains a one-to-one correspondence with the eigenstates of the original Hamiltonian H. In contrast to previously studied square-root lattice models,[56] which are spinless and characterized by Abelian Berry phases, our system incorporates explicit spin degrees of freedom through SOC. Consequently, the topological properties of the system are naturally described within a non-Abelian Berry-phase framework. Upon squaring, the Hamiltonian decomposes into two decoupled effective Hamiltonians in the spin space, facilitating the analysis of the underlying non-Abelian Berry-phase properties and enabling a systematic identification of the topological boundary modes of the original SOC lattice. The squared Hamiltonian in momentum space can be written as

$$H^2(k) = \begin{pmatrix} 4 & 0 & 0 & 0 & 0 & 0 \\ 0 & 4 & 0 & 0 & 0 & 0 \\ 0 & 0 & 2-2\sin k & 0 & 2\cos k & 0 \\ 0 & 0 & 0 & 2+2\sin k & 0 & 2\cos k \\ 0 & 0 & 2\cos k & 0 & 2+2\sin k & 0 \\ 0 & 0 & 0 & 2\cos k & 0 & 2-2\sin k \end{pmatrix}. \tag{7}$$

Since $[H^2, I_3 \otimes \sigma_z] = 0$, the squared Hamiltonian can be block-diagonalized into two independent spin subspaces, corresponding to the spin-up and spin-down sectors, as shown in Fig. 1(d). The resulting Hamiltonians H_+^2 and H_-^2 take the forms

$$H_\pm^2(k) = \begin{pmatrix} 4 & 0 & 0 \\ 0 & 2\mp 2\sin k & 2\cos k \\ 0 & 2\cos k & 2\pm 2\sin k \end{pmatrix}. \tag{8}$$

It is worth noting that the energy of site A is 4 in both sectors and that this site is completely decoupled from the others. The 2×2 sub-block describing the remaining sites B and C can then be written as

$$H^{2'} * \pm(k) = 2\sigma_0 \pm 2\cos k, \sigma_x \mp 2\sin k, \sigma_z, \tag{9}$$

We define the planar vector $\boldsymbol{h}^{2'} * \pm = (\pm 2\cos k, \mp 2\sin k)$, whose winding around the origin as k varies from $-\pi$ to π determines the 1D topological invariant of the subspace, given by

$$v_\pm = \frac{1}{2\pi}\int_{-\pi}^{\pi} \left(\tilde{\boldsymbol{h}} * \pm(k) \times \frac{\mathrm{d}}{\mathrm{d}k} \tilde{\boldsymbol{h}} * \pm(k) \right) \mathrm{d}k = \pm 1, \tag{10}$$

where $\tilde{\boldsymbol{h}} * \pm(k) = \boldsymbol{h} * \pm^{2'}(k)/|\boldsymbol{h}_\pm^{2'}(k)|$. These opposite winding numbers characterize the two topologically distinct sectors corresponding to the spin-up and spin-down subspaces. Although squaring the Hamiltonian maps the $\pm E$ branches onto the same E^2 values, H^2 retains the spatial localization and interference characteristics of the eigenstates of H. Consequently, the topological invariants obtained from H^2 directly reflect the boundary localization and interference-induced features of the original SOC AB cage model.

The spectrum of the squared Hamiltonian H^2 under OBC is shown in Fig. 1(e), featuring two sets of flat bands at $E^2 = 0$ and $E^2 = 4$, along with in-gap boundary states at $E^2 = 2$. The

spatial probability distributions of representative eigenstates are presented in Fig. 1(f). The state at $E^2 = 2$ is localized at the left boundary, identifying it as a topological boundary state. The state at $E^2 = 0$ forms a dark state with vanishing amplitude on all A sites. The state at $E^2 = 4$ exhibits bulk character. These distributions correspond to the characteristic density patterns of the original 1D SOC AB cage model at $E = \pm\sqrt{2}$, $E = 0$, and $E = \pm 2$, confirming that the spatial and boundary features of H are faithfully reflected in H^2.

2.4. Experimental implementation in circuit metamaterials

Classical electrical circuits provide a versatile platform for exploring topological phenomena,[30–34] as their node-based structure allows flexible engineering of lattice connectivity and couplings, while voltages and currents can be directly measured to probe the system response. In such circuits, each node is connected to others through capacitors and inductors, and the current flowing out of node α at frequency ω satisfies Kirchhoff's laws, $I_\alpha(\omega) = J_{\alpha\beta}(\omega)V_\beta(\omega)$, where $V_\beta(\omega)$ is the voltage at node β and $J_{\alpha\beta}(\omega)$ is the circuit Laplacian. Here, capacitive elements contribute $I(\omega) = \mathrm{i}\omega CV(\omega)$, while inductive elements contribute $I(\omega) = (\mathrm{i}\omega L)^{-1}V(\omega)$. Using this framework, we implement the 1D SOC AB cage model by mapping its Hamiltonian onto $J(\omega)$, thereby realizing SOC-induced topological phases in an electrical circuit.

In our circuit design, each lattice site is implemented as a square of four nodes connected by identical capacitors C_0, with nodes labeled $(1,2,3,4)$ as shown in Fig. 2(a), and is realized experimentally on the printed circuit board (PCB) in Fig. 2(c). The n-th unit cell is highlighted by the yellow dashed circle. SOC terms corresponding to σ_x and σ_y are implemented via two distinct interconnection schemes between neighboring sites using identical inductors L, as illustrated in Fig. 2(b). Specifically, for the σ_x coupling, nodes $(1,2,3,4)$ of the a site are connected to $(1,4,3,2)$ of the b site; for the σ_y coupling, they are connected to $(2,1,4,3)$, with the detailed derivation provided in Appendix A. These wiring configurations reproduce the spin-dependent hopping terms of the theoretical 1D SOC AB cage model, ensuring that the circuit faithfully emulates the non-Abelian interference effects in the Hamiltonian. Based on this layout, the circuit Laplacian $J(\omega)$ can be constructed by applying Kirchhoff's laws to each node, yielding the following expression (see Appendix B for more details):

$$\begin{aligned} J(\omega) = & \frac{1}{\mathrm{i}\omega}\sum_n J_n(\omega)\left(a_n^\dagger a_n + b_n^\dagger b_n + c_n^\dagger c_n\right) \\ & -\frac{1}{\mathrm{i}\omega L}\sum_n\Big(\sigma_y a_n^\dagger b_n + \sigma_x a_n^\dagger c_n \\ & +\sigma_y a_n^\dagger c_{n-1} + \sigma_x a_n^\dagger b_{n-1} + \mathrm{h.c.}\Big), \end{aligned} \tag{11}$$

where $J_n(\omega) = \left(-2\omega^2 C_0 + 4/L\right)\sigma_0$. In the absence of external input currents, i.e. $I(\omega) = 0$, the circuit modes satisfy $J(\omega)V(\omega) = -\frac{1}{\mathrm{i}\omega}(H - E(\omega))V(\omega) = 0$, with energy $E(\omega) = -2\omega^2 C_0 + 4/L$. This relation establishes a direct mapping between the circuit Laplacian $J(\omega)$ and the Hamiltonian H of the 1D SOC AB cage model under OBC, such that the eigenmodes of the circuit correspond to the eigenstates of the Hamiltonian and the resonant frequencies encode the energy spectrum. Consequently, the circuit provides a fully controllable platform to experimentally probe the SOC-induced topological states and their associated interference patterns.

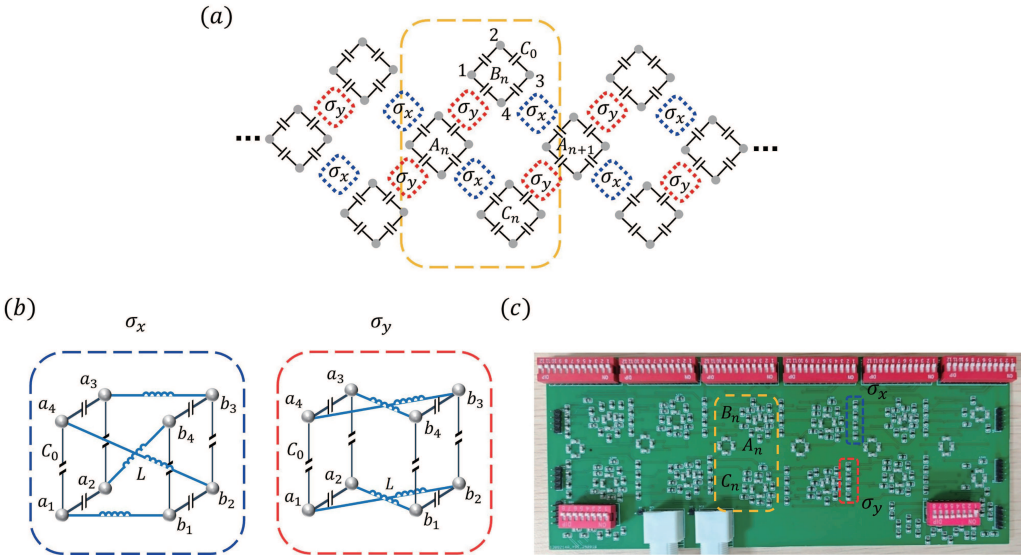


Fig. 2. (a) Schematic of the 1D SOC AB cage circuit lattice, where each lattice site is implemented by a loop of four identical capacitors C_0. (b) The σ_x and σ_y couplings are realized via specific connections of inductors L. (c) Photograph of the experimental PCB, with capacitors $C_0 = 2.2$ nF and inductors $L = 10$ μH.

2.5. Experimental observation of spin-dependent edge modes

In the experiment, we realized a 1D synthetic SOC AB cage with a lattice size of $N = 6$. The theoretical admittance spectrum is shown in Fig. 3(a), where the zeros of the admittance, $j_n(\omega_n) = 0$, correspond to the eigenenergies of the Hamiltonian H through the relation $E_n = -2\omega_n^2 C_0 + 4/L$. Defining $f_n = \omega_n/(2\pi)$, the system exhibits five eigenfrequencies at $f_1 = 1.07$ MHz, $f_2 = 1.21$ MHz, $f_3 = 1.52$ MHz, $f_4 = 1.77$ MHz, and $f_5 = 1.86$ MHz. Among them, f_2 and f_4 correspond to edge states, f_1 and f_5 correspond to bulk states, while f_3 represents a dark state localized inside the SOC AB cage. The eigenstate resonances and their density distributions are experimentally probed by measuring the impedance Z_α between node α and ground. The impedance is related to the eigenvalues and eigenvectors of the circuit Laplacian through $Z_\alpha = \sum_n |\psi_{n,\alpha}|^2/j_n$. This relation implies that, when the circuit is driven at an eigenfrequency, the measured site-resolved impedance becomes proportional to the density distribution of the corresponding eigenstate. It should be noted that, since impedance measurements probe the frequency response at a single site, degenerate states with identical energies cannot be distinguished. Nevertheless, by selectively exciting a specific spin subspace, the states within that subspace can be observed. In the following measurements, we selectively excite the spin-up subspace by driving the four subnodes of each lattice site with the phase pattern $[1, -\mathrm{i}, -1, \mathrm{i}]$ (see Appendix D for details). The measured and simulated impedance responses at sites A_1 (blue), C_1 (red), and B_3 (yellow) over the driving-frequency range from 0 to 3 MHz are shown in Fig. 3(b). Each impedance peak corresponds to an eigenstate with nonzero amplitude at the probed site: all five eigenstates have finite amplitude at site C_1, only the two edge states exhibit finite amplitude at site A_1, and the bulk and dark states exhibit finite amplitude at site B_3. We then measured the impedance at the eigenfrequencies f_2, f_3, and f_4 to probe the spatial density distributions of the edge and dark states in the spin-up sector. As shown in Fig. 3(c), the upper and lower panels present the experimental and simulated results, respectively. For f_2 and f_4, the strong impedance localization at the first unit cell reflects the presence of topological edge states originating from the system's nontrivial SOC. In contrast, at f_3, the response is confined to sites B and C, with vanishing amplitude on site A, confirming the formation of a dark state in which destructive interference between SOC channels prevents energy transfer through site A. The experimental results are in excellent agreement with simulations.

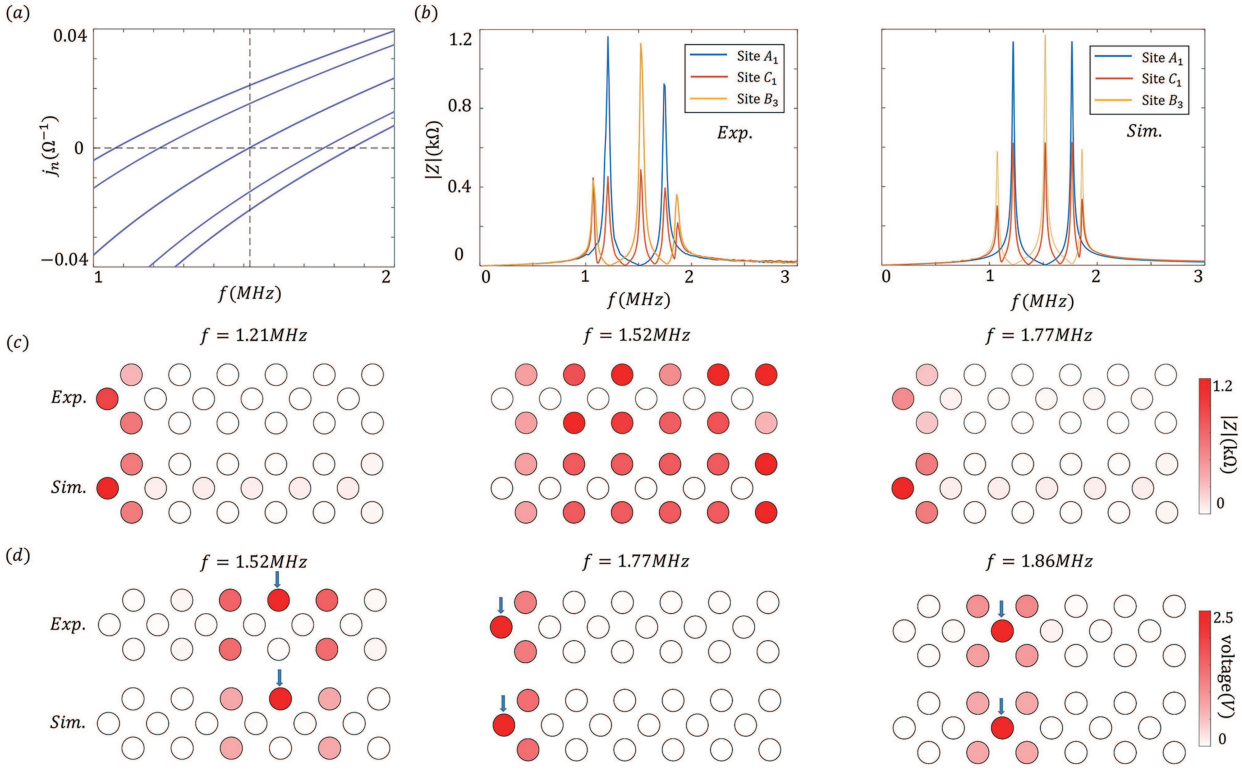


Fig. 3. (a) Admittance spectrum of the effective circuit Laplacian $J(\omega)$, showing five eigenfrequencies at $f_n = 1.07, 1.21, 1.52, 1.77$, and 1.86 MHz, with the mode at $f_3 = 1.52$ MHz (crosshair) corresponding to the zero-energy dark state. (b) Measured (left) and simulated (right) impedance at sites A_1 (blue), C_1 (red), and B_3 (yellow) to ground, obtained by scanning the driving frequency from 0 to 3 MHz. (c) Experimental (top) and simulated (bottom) impedance distributions at f_2 and f_4 (boundary states) and f_3 (dark state). (d) Experimental (top) and simulated (bottom) voltage distributions under local excitations at site B_4 for the dark state at f_3, at site A_1 for the edge state at f_4, and at site A_3 for the bulk state at f_5. In panels (b)–(d), the measurements and simulations are performed by selectively exciting the spin-up sector.

Furthermore, to directly probe the spatial localization of the flat-band modes, we performed site-selective excitations in the spin-up sector by exciting nodes B_4, A_1, and A_3 at the eigenfrequencies f_3 (dark state), f_4 (edge state), and f_5 (bulk state), respectively. Each excitation used an AC voltage of 2.5 V, and the resulting steady-state voltage profiles across the lattice are shown in Fig. 3(d). This site-selective driving approach ensures that the excited node predominantly couples to the eigenmode with the largest local amplitude, enabling a clear visualization of the underlying density distributions. The measurements reveal that the dark state is confined to the B and C sites of three adjacent unit cells and exhibits a vanishing amplitude at the C site of the driven cell due to destructive interference. The edge state remains confined within the first unit cell, as expected for this boundary-localized mode. By contrast, the bulk state spreads over five unit cells centered around the A site, with reduced voltage on neighboring A sites resulting from SOC-induced interference patterns. All measured voltage profiles show excellent agreement with circuit simulations. To further verify the robustness of the SOC-induced topological phase, we present simulations with a 10% parameter deviation in Appendix G. The results show that the topological phase remains stable within this error range. In addition, control measurements performed with spin-down excitation yield identical spatial impedance and voltage distribution profiles.

3. Spinful second-order topological phase in a dimer SOC lattice

3.1. Theoretical model

We extend the SOC AB cage model to two dimensions, forming the lattice illustrated in Fig. 4(a). The lattice incorporates SOC σ_x and σ_y along the x and y directions, generating an effective π-flux per plaquette. Each unit cell comprises four sites, A, B, C, and D (yellow dashed box), with intra-cell hopping t_1 and inter-cell hopping t_2. The resulting Hamiltonian in momentum space describes a two-dimensional SOC system exhibiting second-order topological properties, characterized by gapped bulk and edge spectra and the emergence of topological corner states.[57–101] Importantly, distinct from the seminal Benalcazar–Bernevig–Hughes (BBH) model,[57] which is defined on a two-dimensional square lattice with dimerized hoppings along both spatial directions and a π-flux threaded through each plaquette, our lattice model is constructed purely from dimerized spin–orbit couplings. In this setting, no synthetic π-flux gauge field is required to realize higher-order topology. Even in the absence of a π-flux, the SOC-induced dimerization supports in-gap topological corner modes and leads to a doubling of the corner-state multiplicity compared with the BBH model. Its explicit form in momentum space is given by

$$\begin{aligned} H(k_x,k_y) &= (t_1+t_2\cos k_x)\Lambda_1+(t_1+t_2\cos k_y)\Lambda_2 \\ &\quad -t_2\sin k_x\Lambda_3-t_2\sin k_y\Lambda_4, \end{aligned} \tag{12}$$

where $\Lambda_1=\varsigma_x\tau_0\sigma_x$, $\Lambda_2=\varsigma_x\tau_x\sigma_y$, $\Lambda_3=\varsigma_y\tau_z\sigma_x$, and $\Lambda_4=\varsigma_x\tau_y\sigma_y$, with each Λ_i explicitly defined as the tensor product $\varsigma_i\otimes\tau_j\otimes\sigma_k$ of three Pauli matrices. The Hamiltonian possesses mirror symmetry with respect to the line $k_x=k_y$, generated by the operator $M_{xy}=\tau_0\sigma_y\oplus\tau_x\sigma_x$. Under this mirror operation, the Hamiltonian satisfies $M_{xy}H(k_x,k_y)M_{xy}^{\dagger}=H(k_y,k_x)$. Additionally, the system preserves chiral symmetry, with the chiral operator $C=\varsigma_z\tau_0\sigma_0$, which satisfies $CH(k_x,k_y)C^{-1}=-H(k_x,k_y)$.

To investigate the topological corner modes under OBC, we next consider the system in real space. The Hamiltonian of the model in real space is given as

$$\begin{aligned} H &= \sum_{m,n}\Big(t_1\sigma_x a_{m,n}^{\dagger}c_{m,n}+t_1\sigma_x b_{m,n}^{\dagger}d_{m,n}+t_1\sigma_y a_{m,n}^{\dagger}d_{m,n} \\ &\quad +t_1\sigma_y b_{m,n}^{\dagger}c_{m,n}+t_2\sigma_x a_{m,n}^{\dagger}c_{m-1,n}+t_2\sigma_x d_{m,n}^{\dagger}b_{m-1,n} \\ &\quad +t_2\sigma_y a_{m,n}^{\dagger}d_{m,n-1}+t_2\sigma_y c_{m,n}^{\dagger}b_{m,n-1}+\text{h.c.}\Big), \end{aligned} \tag{13}$$

where $a_{m,n}^{\dagger}(b_{m,n}^{\dagger},c_{m,n}^{\dagger},d_{m,n}^{\dagger})$ and $a_{m,n}(b_{m,n},c_{m,n},d_{m,n})$ are the creation and annihilation operators at A (B, C, and D), respectively. Owing to chiral symmetry, the Hamiltonian can be transformed into the block-off-diagonal form

$$H=\begin{pmatrix}0 & h\\ h^{\dagger} & 0\end{pmatrix}, \tag{14}$$

which naturally partitions the lattice into two sublattices A and B that carry opposite chiral charges. In the one-dimensional SOC AB-cage model, squaring the Hamiltonian produces decoupled subspaces, which enables the square-root construction. Although the two-dimensional SOC higher-order model possesses chiral symmetry and exhibits local cage-like interference effects, it does not allow such a decomposition, and the square-root framework is therefore inapplicable. Instead, its second-order topology is characterized by a multipole chiral number, which is protected by crystalline symmetries. We introduce quadrupole-moment operators Q_{ij}^{A} and Q_{ij}^{B} acting on the subspaces associated with sublattices A and B, respectively. After projecting onto their occupied-band subspaces using U_A and U_B, their reduced forms are $\bar{Q}*ij^{S}=U_S^{\dagger}Q*ij^{S}U_S$, $S\in A,B$. The 2D multipole chiral number is then defined as[102]

$$N=\frac{1}{2\pi\mathrm{i}}\,\mathrm{Tr}\log\left(\bar{Q}*ij^{A}\bar{Q}*ij^{B\dagger}\right)\in\mathbb{Z}. \tag{15}$$

In our system, when $t_2/t_1<1$, the topological index $N=0$ indicates a trivial phase. As t_2/t_1 increases and crosses the critical point $t_1=t_2$, the system undergoes a topological transition. For $t_2/t_1>1$, the topological index becomes $N=2$,

showing that the system enters a nontrivial phase (phase diagram see Appendix E). In this case, two degenerate zero-energy modes localize at each of the four crystalline corners under OBC, forming eight degenerate corner states.

We construct a 2D SOC lattice with 4×4 unit cells under OBC to probe higher-order topological features. The corresponding energy spectrum is shown in Fig. 4(b). In the trivial phase (top panel), the spectrum consists of two symmetric bulk bands (black) separated by a gap, with no in-gap states, indicating the absence of topologically protected boundary modes. In contrast, in the topological phase (bottom panel), the bulk-boundary correspondence ensures the emergence of topological boundary states. The spectrum clearly separates into three sectors: in-gap corner states (red), 1D edge states along the lattice boundaries (blue), and conventional bulk states (black). The corner states are zero-dimensional modes localized at the lattice vertices, directly reflecting the nontrivial bulk topology characteristic of the SOC SOTI. The edge states extend along the 1D boundaries connecting the corners, forming topologically protected 1D channels. The bulk states remain delocalized across the lattice, as expected for conventional bands. These spatial features are further confirmed by the real-space probability density distributions in Fig. 4(c), where the top, middle, and bottom panels correspond to corner, edge, and bulk states, respectively.

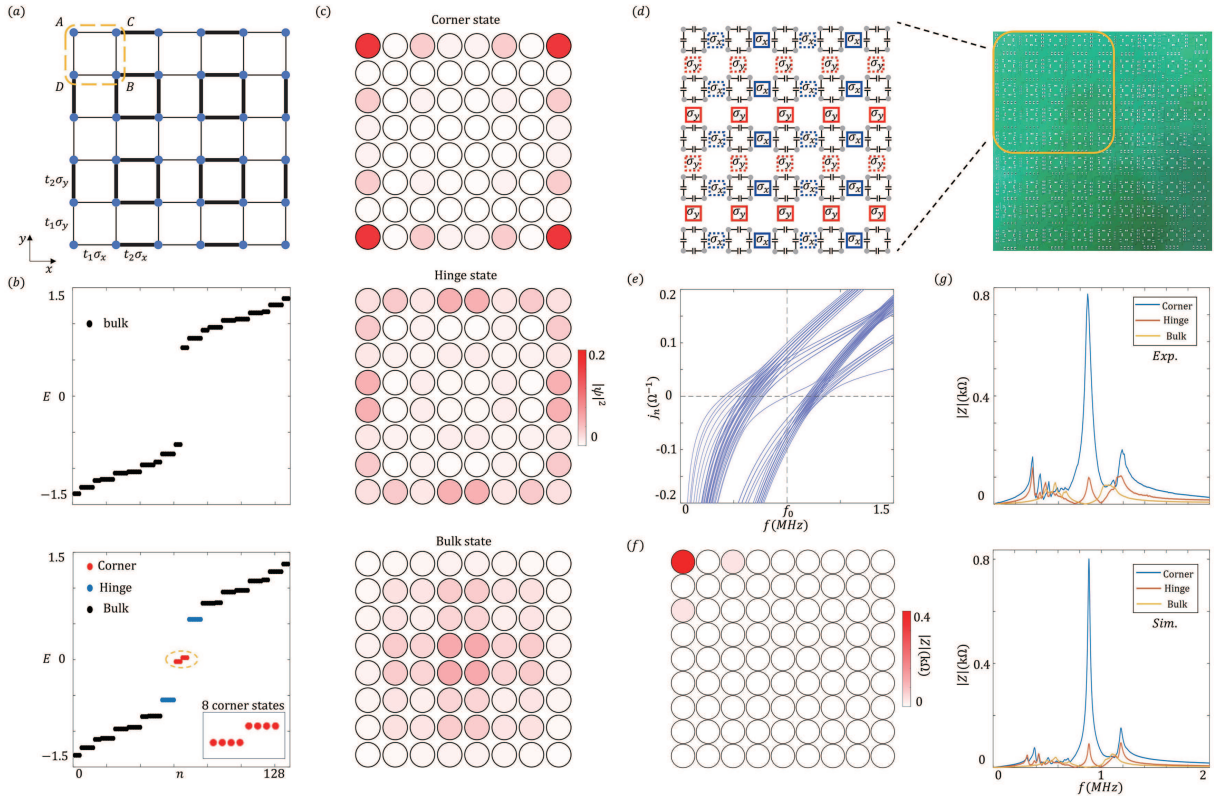


Fig. 4. (a) Schematic of the 2D SOC SOTI lattice with σ_x couplings along x and σ_y couplings along y, where the intercell and intracell hopping strengths are t_1 and t_2, respectively. (b) Energy spectra of a 4×4 lattice under open boundary conditions: trivial phase ($t_1 = 0.7, t_2 = 0.3$, top) with bulk (black) states, and topological phase ($t_1 = 0.3, t_2 = 0.7$, bottom) with bulk (black), edge (blue), and in-gap corner (red) states. The enlarged sub-image at the bottom right shows the eight corner states. (c) Density distributions in the topological phase: corner (top), edge (middle), and bulk (bottom) states. (d) Circuit schematic and experimental PCB. (e) Theoretical admittance spectrum with the corner state within the gap at f_0. (f) Impedance distribution of the corner state at the resonant frequency f_0 under spin-up excitation. (g) Experimental (top) and simulated (bottom) impedance spectra measured at corner, edge, and bulk sites under spin-up excitation over the frequency range from 0 to 2 MHz, with the corner-state resonance at f_0 clearly isolated from the bulk and edge bands. The circuit components are chosen as $C_1 = 3.3$ nF, $L_1 = 10$ μH, and $L_2 = 3.3$ μH, yielding a resonant frequency $f_0 = 1/(2\pi\sqrt{C_1 L_1}) \approx 876$ kHz.

3.2. Circuit implementation in circuit metamaterials

For the experimental realization of corner states in the synthetic SOC SOTI model, we designed a standard PCB comprising 4.5×4.5 unit cells, as shown in Fig. 4(d). The yellow circle highlights an enlarged schematic of the underlying circuit network, illustrating the detailed layout of nodes and interconnections. Analogous to the 1D SOC AB cage model, the synthetic SOC along the x and y directions is implemented through specific interconnection patterns of inductors, corresponding to σ_x (blue boxes) and σ_y (red boxes), respectively. The intra-cell and inter-cell inductances, L_1 (dashed lines) and L_2 (solid lines), establish dimerized hopping amplitudes, allowing precise control of the SOC strengths. This design enables the realization of higher-order topological phases and supports corner-localized modes as predicted theoretically. To guarantee uniform resonance across all nodes, differentiated

grounding conditions are applied to satisfy the resonance relation $\omega_0 = \sqrt{\frac{1}{C_1 L_1}} = \sqrt{\frac{1}{C_2 L_2}}$, where C_1 denotes the coupling capacitor connecting the four loops within a unit cell, and C_2 represents an additional compensation capacitor introduced through the grounding configuration (see Appendix C for details). This ensures that all unit cells and their constituent nodes oscillate coherently at the target frequency ω_0, minimizing detuning effects and preserving the designed SOC interference patterns. Applying Kirchhoff's laws to each node, the corresponding circuit Laplacian $J(\omega_0)$ can be constructed, which directly maps onto the theoretical Hamiltonian of the 2D SOC SOTI model (see Appendix B for details)

$$\begin{aligned} J(\omega_0) = \frac{1}{\mathrm{i}\omega_0}\sum_{m,n}\Bigg(&-\frac{1}{L_1}\sigma_x a^{\dagger}_{m,n}c_{m,n} - \frac{1}{L_1}\sigma_x b^{\dagger}_{m,n}d_{m,n} \\ &-\frac{1}{L_1}\sigma_y a^{\dagger}_{m,n}d_{m,n} - \frac{1}{L_1}\sigma_y b^{\dagger}_{m,n}c_{m,n} \\ &-\frac{1}{L_2}\sigma_x a^{\dagger}_{m,n}c_{m-1,n} - \frac{1}{L_2}\sigma_x d^{\dagger}_{m,n}b_{m-1,n} \\ &-\frac{1}{L_2}\sigma_y a^{\dagger}_{m,n}d_{m,n-1} - \frac{1}{L_2}\sigma_y c^{\dagger}_{m,n}b_{m,n-1} + \mathrm{h.c.}\Bigg). \end{aligned} \tag{16}$$

The SOC SOTI Hamiltonian H is directly obtained from the circuit Laplacian via $J(\omega_0) = 1/(\mathrm{i}\omega_0)H$, with the intra-cell and inter-cell coupling strengths set by $t_1 = 1/L_1$ and $t_2 = 1/L_2$, respectively. This PCB implementation thus provides a faithful realization of the theoretical SOC SOTI model, enabling direct experimental access to corner-localized modes and the exploration of their higher-order topological properties.

3.3. Experimental observation of spin-dependent corner modes

We theoretically calculate the dependence of the spectrum of the circuit Laplacian on the driving frequency, as shown in Fig. 4(e). An isolated mode traverses the bandgap and reaches zero at the resonant frequency f_0, corresponding to a zero eigenvalue of the Laplacian ($j_n = 0$). This mode represents a corner-localized, zero-admittance state, whose existence is protected by the higher-order topology of the system. Its presence within the bulk bandgap provides a clear theoretical indication of topological corner modes in the SOC SOTI circuit and highlights the nontrivial bulk–boundary correspondence. For comparison, we also provide simulations of the trivial phase in Appendix F.

To experimentally probe the spatially resolved response of the lattice, we applied an AC voltage over the frequency range from 0 to 2 MHz and measured the impedance spectra at representative corner, edge, and bulk sites in the spin-up sector, as shown in Fig. 4(g). At the resonant frequency f_0, the corner site exhibits a pronounced impedance peak, indicating strong localization of the excitation, whereas the edge and bulk sites display only weak responses. This site-dependent resonance behavior directly reflects the spatial confinement of the corner mode and confirms its selective occupation of the lattice corner. The experimental results show excellent agreement with numerical simulations based on the same circuit parameters, validating both the circuit design and the theoretical predictions.

Furthermore, the spatial impedance distribution measured in the spin-up sector at the resonant frequency f_0, shown in Fig. 4(f), exhibits a sharply localized pattern at a single corner, with the response rapidly decaying away from this site. This observation provides direct experimental evidence for the existence of a higher-order topological corner state. The corner mode demonstrates strong spatial localization and robustness against perturbations in the surrounding lattice, consistent with the predictions of higher-order topological theory. Together, these results unambiguously confirm the realization of 2D SOC-induced SOTI corner states and their characteristic higher-order topological properties in the electrical circuit platform. Measurements performed with spin-down excitation lead to the same spectral features and spatial localization profiles.

4. Conclusion

In summary, we have shown that SOC-induced spin-dependent interference enriches boundary physics in low-dimensional lattice systems. In one dimension, it simultaneously produces AB caging of bulk states and square-root topological boundary modes. In two dimensions, SOC gives rise to higher-order topological corner states that are robustly localized at lattice corners and protected by gapped edges, highlighting the role of SOC in enriching boundary physics within established topological frameworks. Experimental observations confirm the predicted localization and robustness of both bulk and boundary states, providing direct evidence that interference can reorganize and enrich topological boundary states in engineered lattice systems. Looking forward, our work offers a new theoretical perspective for exploring SOC-enriched synthetic topological phases and enables spin-dependent topological boundary structures. In addition to these fundamental insights, topological circuit metamaterials are inherently compatible with complementary metal–oxide–semiconductor technology and have shown promising applications in wireless signal processing[103] and ultrasensitive circuit-based sensors.[104,105] Here, we demonstrate that synthetic SOC can induce and enrich topological phases by introducing an additional pseudospin degree of freedom. This capability enables pseudospin-dependent functionalities, allowing the design of robust, selective, or multifunctional devices, such as pseudospin-selective filters, signal processors, and electromagnetic sensors.

Appendix A: Circuit implementation of synthetic SOC

In this section, we provide a detailed derivation of the SOC terms associated with the operators σ_x and σ_y. Consider the circuit configuration shown in Fig. 2(b). Applying Kirchhoff's current law to the nodes in the σ_x configuration yields

$$\begin{aligned}
I_{a,1} &= \mathrm{i}\omega C_0(V_{a,1}-V_{a,2})+\mathrm{i}\omega C_0(V_{a,1}-V_{a,4})\\
&\quad+\frac{1}{\mathrm{i}\omega L}(V_{a,1}-V_{b,1}),\\
I_{a,2} &= \mathrm{i}\omega C_0(V_{a,2}-V_{a,1})+\mathrm{i}\omega C_0(V_{a,2}-V_{a,3})\\
&\quad+\frac{1}{\mathrm{i}\omega L}(V_{a,2}-V_{b,4}),\\
I_{a,3} &= \mathrm{i}\omega C_0(V_{a,3}-V_{a,2})+\mathrm{i}\omega C_0(V_{a,3}-V_{a,4})\\
&\quad+\frac{1}{\mathrm{i}\omega L}(V_{a,3}-V_{b,3}),\\
I_{a,4} &= \mathrm{i}\omega C_0(V_{a,4}-V_{a,1})+\mathrm{i}\omega C_0(V_{a,4}-V_{a,3})\\
&\quad+\frac{1}{\mathrm{i}\omega L}(V_{a,4}-V_{b,2}),\\
I_{b,1} &= \mathrm{i}\omega C_0(V_{b,1}-V_{b,2})+\mathrm{i}\omega C_0(V_{b,1}-V_{b,4})\\
&\quad+\frac{1}{\mathrm{i}\omega L}(V_{b,1}-V_{a,1}),\\
I_{b,2} &= \mathrm{i}\omega C_0(V_{b,2}-V_{b,1})+\mathrm{i}\omega C_0(V_{b,2}-V_{b,3})\\
&\quad+\frac{1}{\mathrm{i}\omega L}(V_{b,2}-V_{a,4}),\\
I_{b,3} &= \mathrm{i}\omega C_0(V_{b,3}-V_{b,2})+\mathrm{i}\omega C_0(V_{b,3}-V_{b,4})\\
&\quad+\frac{1}{\mathrm{i}\omega L}(V_{b,3}-V_{a,3}),\\
I_{b,4} &= \mathrm{i}\omega C_0(V_{b,4}-V_{b,1})+\mathrm{i}\omega C_0(V_{b,4}-V_{b,3})\\
&\quad+\frac{1}{\mathrm{i}\omega L}(V_{b,4}-V_{a,2}).
\end{aligned}\tag{A1}$$

Here, $I_{a(b),j}$ and $V_{a(b),j}$ $(j=1,2,3,4)$ denote the current and voltage at node j of site $a(b)$, respectively. We define the current and voltage vectors as $I_{a(b)}=[I_{a(b),1},I_{a(b),2},I_{a(b),3},I_{a(b),4}]^{\mathrm{T}}$ and $V_{a(b)}=[V_{a(b),1},V_{a(b),2},V_{a(b),3},V_{a(b),4}]^{\mathrm{T}}$. The above node equations can be compactly rewritten in matrix form as

$$\begin{bmatrix}I_a\\I_b\end{bmatrix}=\begin{bmatrix}\mathrm{i}\omega C_0M_0+\dfrac{1}{\mathrm{i}\omega L} & \dfrac{-1}{\mathrm{i}\omega L}M_x\\ \dfrac{-1}{\mathrm{i}\omega L}M_x & \mathrm{i}\omega C_0M_0+\dfrac{1}{\mathrm{i}\omega L}\end{bmatrix}\begin{bmatrix}V_a\\V_b\end{bmatrix},\tag{A2}$$

where M_0 and M_x represent the pseudo-spin matrix and the σ_x coupling matrix, respectively. The explicit forms of these matrices are given by

$$M_0=\begin{bmatrix}2&-1&0&-1\\-1&2&-1&0\\0&-1&2&-1\\-1&0&-1&2\end{bmatrix},\ M_x=\begin{bmatrix}1&0&0&0\\0&0&0&1\\0&0&1&0\\0&1&0&0\end{bmatrix}.\tag{A3}$$

By applying a unitary transformation U to diagonalize the matrices M_0 and M_x, we obtain

$$\begin{aligned}
U&=\frac{1}{2}\begin{bmatrix}1&1&1&1\\1&-1&1&-1\\1&-\mathrm{i}&-1&\mathrm{i}\\1&\mathrm{i}&-1&-\mathrm{i}\end{bmatrix},\\
U^{\dagger}M_0U&=\begin{bmatrix}0&0\\0&4\end{bmatrix}\oplus 2\sigma_0,\ \ U^{\dagger}M_xU=\sigma_0\oplus\sigma_x.
\end{aligned}\tag{A4}$$

Thus, the Laplacian matrix between a and b is

$$\begin{bmatrix}I_a\\I_b\end{bmatrix}=\begin{bmatrix}K & \frac{-1}{\mathrm{i}\omega L}(\sigma_0\oplus\sigma_x)\\ \frac{-1}{\mathrm{i}\omega L}(\sigma_0\oplus\sigma_x) & K\end{bmatrix}\begin{bmatrix}V_a\\V_b\end{bmatrix},\tag{A5}$$

where $K=\mathrm{i}\omega C_0\left(\begin{bmatrix}0&0\\0&4\end{bmatrix}\oplus 2\sigma_0\right)+\frac{1}{\mathrm{i}\omega L}$. We define the spin-space representation of the node voltages for sites a and b as

$$V'_{a(b)}=\begin{bmatrix}V_{a(b),\uparrow}\\V_{a(b),\downarrow}\end{bmatrix}=\begin{bmatrix}V_{a(b),1}-\mathrm{i}V_{a(b),2}-V_{a(b),3}+\mathrm{i}V_{a(b),4}\\V_{a(b),1}+\mathrm{i}V_{a(b),2}-V_{a(b),3}-\mathrm{i}V_{a(b),4}\end{bmatrix}.\tag{A6}$$

The corresponding currents in this spin basis are denoted by $I'_{a(b)}$, and the Laplacian matrix describing the coupling between sites a and b is then written as

$$\begin{bmatrix}I'_a\\I'_b\end{bmatrix}=\begin{bmatrix}(2\mathrm{i}\omega C_0+\dfrac{1}{\mathrm{i}\omega L})\sigma_0 & \dfrac{-1}{\mathrm{i}\omega L}\sigma_x\\ \dfrac{-1}{\mathrm{i}\omega L}\sigma_x & (2\mathrm{i}\omega C_0+\dfrac{1}{\mathrm{i}\omega L})\sigma_0\end{bmatrix}\begin{bmatrix}V'_a\\V'_b\end{bmatrix}.\tag{A7}$$

It is clear that the inter-site coupling between a and b directly implements the spin–orbit coupling term σ_x in this spin-space representation. This formulation allows a transparent mapping between the physical circuit and the effective SOC Hamiltonian.

Similarly, for the σ_y configuration, the Kirchhoff equations for nodes a and b can be written as

$$\begin{bmatrix}I_a\\I_b\end{bmatrix}=\begin{bmatrix}\mathrm{i}\omega C_0M_0+\dfrac{1}{\mathrm{i}\omega L} & \dfrac{-1}{\mathrm{i}\omega L}M_y\\ \dfrac{-1}{\mathrm{i}\omega L}M_y & \mathrm{i}\omega C_0M_0+\dfrac{1}{\mathrm{i}\omega L}\end{bmatrix}\begin{bmatrix}V_a\\V_b\end{bmatrix},\tag{A8}$$

where M_y represents the σ_y coupling matrix. The explicit forms of the matrices and their representations after block diagonalization via the unitary transformation U are given by

$$M_y=\begin{bmatrix}0&1&0&0\\1&0&0&0\\0&0&0&1\\0&0&1&0\end{bmatrix},\ \ U^{\dagger}M_yU=\sigma_z\oplus\sigma_y.\tag{A9}$$

Thus, the Laplacian matrix between a and b is

$$\begin{bmatrix}I'_a\\I'_b\end{bmatrix}=\begin{bmatrix}(2\mathrm{i}\omega C_0+\dfrac{1}{\mathrm{i}\omega L})\sigma_0 & \dfrac{-1}{\mathrm{i}\omega L}\sigma_y\\ \dfrac{-1}{\mathrm{i}\omega L}\sigma_y & (2\mathrm{i}\omega C_0+\dfrac{1}{\mathrm{i}\omega L})\sigma_0\end{bmatrix}\begin{bmatrix}V'_a\\V'_b\end{bmatrix}.\tag{A10}$$

It is clear that the coupling between a and b in this case realizes the SOC term σ_y.

Appendix B: Derivation of the circuit Laplacian

We now derive the Laplacian matrix of the LC circuit implementing the 1D SOC AB cage. The Kirchhoff equations for the A, B, and C sites of the n-th unit cell are

$$\begin{aligned}
I_a^n &= \mathrm{i}\omega C_0 M_0 V_a^n + \frac{1}{\mathrm{i}\omega L}\left(V_a^n - M_y V_b^n\right) \\
&\quad + \frac{1}{\mathrm{i}\omega L}\left(V_a^n - M_x V_c^n\right) + \frac{1}{\mathrm{i}\omega L}\left(V_a^n - M_x V_b^{n-1}\right) \\
&\quad + \frac{1}{\mathrm{i}\omega L}\left(V_a^n - M_y V_c^{n-1}\right), \\
I_b^n &= \mathrm{i}\omega C_0 M_0 V_b^n + \frac{2}{\mathrm{i}\omega L} V_b^n + \frac{1}{\mathrm{i}\omega L}\left(V_b^n - M_y V_a^n\right) \\
&\quad + \frac{1}{\mathrm{i}\omega L}\left(V_b^n - M_x V_a^{n+1}\right), \\
I_c^n &= \mathrm{i}\omega C_0 M_0 V_c^n + \frac{2}{\mathrm{i}\omega L} V_c^n + \frac{1}{\mathrm{i}\omega L}\left(V_c^n - M_x V_a^n\right) \\
&\quad + \frac{1}{\mathrm{i}\omega L}\left(V_c^n - M_y V_a^{n+1}\right), \qquad \text{(B1)}
\end{aligned}$$

where $I_i^n = \left[I_{i,1}^n, I_{i,2}^n, I_{i,3}^n, I_{i,4}^n\right]$ and $V_i^n = \left[V_{i,1}^n, V_{i,2}^n, V_{i,3}^n, V_{i,4}^n\right]$ are the current and voltage vectors at site i ($i = a, b, c$), respectively. Simplifying the above equations, we obtain

$$\begin{aligned}
I_a^n &= \left(\mathrm{i}\omega C_0 M_0 + \frac{4}{\mathrm{i}\omega L}\right) V_a^n \\
&\quad - \frac{1}{\mathrm{i}\omega L}\left[M_y(V_b^n + V_c^{n-1}) + M_x(V_b^{n-1} + V_c^n)\right], \\
I_b^n &= \left(\mathrm{i}\omega C_0 M_0 + \frac{4}{\mathrm{i}\omega L}\right) V_b^n - \frac{1}{\mathrm{i}\omega L}\left(M_y V_a^n + M_x V_a^{n+1}\right), \\
I_c^n &= \left(\mathrm{i}\omega C_0 M_0 + \frac{4}{\mathrm{i}\omega L}\right) V_c^n - \frac{1}{\mathrm{i}\omega L}\left(M_x V_a^n + M_y V_a^{n+1}\right). \qquad \text{(B2)}
\end{aligned}$$

Using the unitary transformation U, we obtain the following expressions in the spin subspace

$$\begin{aligned}
\begin{bmatrix} I_{a\uparrow}^n \\ I_{a\downarrow}^n \end{bmatrix} &= \left(2\mathrm{i}\omega C_0 + \frac{4}{\mathrm{i}\omega L}\right)\sigma_0 \begin{bmatrix} V_{a\uparrow}^n \\ V_{a\downarrow}^n \end{bmatrix} - \frac{1}{\mathrm{i}\omega L}\sigma_y \begin{bmatrix} V_{b\uparrow}^n \\ V_{b\downarrow}^n \end{bmatrix} \\
&\quad - \frac{1}{\mathrm{i}\omega L}\sigma_x \begin{bmatrix} V_{c\uparrow}^n \\ V_{c\downarrow}^n \end{bmatrix} - \frac{1}{\mathrm{i}\omega L}\sigma_x \begin{bmatrix} V_{b\uparrow}^{n-1} \\ V_{b\downarrow}^{n-1} \end{bmatrix} \\
&\quad - \frac{1}{\mathrm{i}\omega L}\sigma_y \begin{bmatrix} V_{c\uparrow}^{n-1} \\ V_{c\downarrow}^{n-1} \end{bmatrix}, \\
\begin{bmatrix} I_{b\uparrow}^n \\ I_{b\downarrow}^n \end{bmatrix} &= \left(2\mathrm{i}\omega C_0 + \frac{4}{\mathrm{i}\omega L}\right)\sigma_0 \begin{bmatrix} V_{b\uparrow}^n \\ V_{b\downarrow}^n \end{bmatrix} - \frac{1}{\mathrm{i}\omega L}\sigma_y \begin{bmatrix} V_{a\uparrow}^n \\ V_{a\downarrow}^n \end{bmatrix} \\
&\quad - \frac{1}{\mathrm{i}\omega L}\sigma_x \begin{bmatrix} V_{a\uparrow}^{n+1} \\ V_{a\downarrow}^{n+1} \end{bmatrix}, \\
\begin{bmatrix} I_{c\uparrow}^n \\ I_{c\downarrow}^n \end{bmatrix} &= \left(2\mathrm{i}\omega C_0 + \frac{4}{\mathrm{i}\omega L}\right)\sigma_0 \begin{bmatrix} V_{c\uparrow}^n \\ V_{c\downarrow}^n \end{bmatrix} - \frac{1}{\mathrm{i}\omega L}\sigma_x \begin{bmatrix} V_{a\uparrow}^n \\ V_{a\downarrow}^n \end{bmatrix} \\
&\quad - \frac{1}{\mathrm{i}\omega L}\sigma_y \begin{bmatrix} V_{a\uparrow}^{n+1} \\ V_{a\downarrow}^{n+1} \end{bmatrix}. \qquad \text{(B3)}
\end{aligned}$$

We can then obtain the Laplacian matrix $J(\omega)$

$$\begin{aligned}
J(\omega) &= \frac{1}{\mathrm{i}\omega}\sum_n J_n(\omega)\left(a_n^\dagger a_n + b_n^\dagger b_n + c_n^\dagger c_n\right) \\
&\quad - \frac{1}{\mathrm{i}\omega L}\sum_n \Big(\sigma_y a_n^\dagger b_n + \sigma_x a_n^\dagger c_n \\
&\quad + \sigma_y a_n^\dagger c_{n-1} + \sigma_x a_n^\dagger b_{n-1} + \text{h.c.}\Big). \qquad \text{(B4)}
\end{aligned}$$

Extending the 1D derivation, we derive the Kirchhoff equations for the 2D LC circuit. The circuit relations for the lattice sites a, b, c, and d are given by

$$\begin{aligned}
\begin{bmatrix} I_{a\uparrow}^{m,n} \\ I_{a\downarrow}^{m,n} \end{bmatrix} &= \left[2\mathrm{i}\omega C_1 + \frac{2}{\mathrm{i}\omega}\left(\frac{1}{L_1} + \frac{1}{L_2}\right)\right]\sigma_0 \begin{bmatrix} V_{a\uparrow}^{m,n} \\ V_{a\downarrow}^{m,n} \end{bmatrix} \\
&\quad - \frac{1}{\mathrm{i}\omega L_1}\sigma_x \begin{bmatrix} V_{c\uparrow}^{m,n} \\ V_{c\downarrow}^{m,n} \end{bmatrix} - \frac{1}{\mathrm{i}\omega L_1}\sigma_y \begin{bmatrix} V_{d\uparrow}^{m,n} \\ V_{d\downarrow}^{m,n} \end{bmatrix} \\
&\quad - \frac{1}{\mathrm{i}\omega L_2}\sigma_x \begin{bmatrix} V_{c\uparrow}^{m-1,n} \\ V_{c\downarrow}^{m-1,n} \end{bmatrix} - \frac{1}{\mathrm{i}\omega L_2}\sigma_y \begin{bmatrix} V_{d\uparrow}^{m,n-1} \\ V_{d\downarrow}^{m,n-1} \end{bmatrix}, \\
\begin{bmatrix} I_{b\uparrow}^{m,n} \\ I_{b\downarrow}^{m,n} \end{bmatrix} &= \left[2\mathrm{i}\omega C_1 + \frac{2}{\mathrm{i}\omega}\left(\frac{1}{L_1} + \frac{1}{L_2}\right)\right]\sigma_0 \begin{bmatrix} V_{b\uparrow}^{m,n} \\ V_{b\downarrow}^{m,n} \end{bmatrix} \\
&\quad - \frac{1}{\mathrm{i}\omega L_1}\sigma_x \begin{bmatrix} V_{d\uparrow}^{m,n} \\ V_{d\downarrow}^{m,n} \end{bmatrix} - \frac{1}{\mathrm{i}\omega L_1}\sigma_y \begin{bmatrix} V_{c\uparrow}^{m,n} \\ V_{c\downarrow}^{m,n} \end{bmatrix} \\
&\quad - \frac{1}{\mathrm{i}\omega L_2}\sigma_x \begin{bmatrix} V_{d\uparrow}^{m-1,n} \\ V_{d\downarrow}^{m-1,n} \end{bmatrix} - \frac{1}{\mathrm{i}\omega L_2}\sigma_y \begin{bmatrix} V_{c\uparrow}^{m,n-1} \\ V_{c\downarrow}^{m,n-1} \end{bmatrix}, \\
\begin{bmatrix} I_{c\uparrow}^{m,n} \\ I_{c\downarrow}^{m,n} \end{bmatrix} &= \left[2\mathrm{i}\omega C_1 + \frac{2}{\mathrm{i}\omega}\left(\frac{1}{L_1} + \frac{1}{L_2}\right)\right]\sigma_0 \begin{bmatrix} V_{c\uparrow}^{m,n} \\ V_{c\downarrow}^{m,n} \end{bmatrix} \\
&\quad - \frac{1}{\mathrm{i}\omega L_1}\sigma_x \begin{bmatrix} V_{a\uparrow}^{m,n} \\ V_{a\downarrow}^{m,n} \end{bmatrix} - \frac{1}{\mathrm{i}\omega L_1}\sigma_y \begin{bmatrix} V_{b\uparrow}^{m,n} \\ V_{b\downarrow}^{m,n} \end{bmatrix} \\
&\quad - \frac{1}{\mathrm{i}\omega L_2}\sigma_x \begin{bmatrix} V_{a\uparrow}^{m-1,n} \\ V_{a\downarrow}^{m-1,n} \end{bmatrix} - \frac{1}{\mathrm{i}\omega L_2}\sigma_y \begin{bmatrix} V_{b\uparrow}^{m,n-1} \\ V_{b\downarrow}^{m,n-1} \end{bmatrix}, \\
\begin{bmatrix} I_{d\uparrow}^{m,n} \\ I_{d\downarrow}^{m,n} \end{bmatrix} &= \left[2\mathrm{i}\omega C_1 + \frac{2}{\mathrm{i}\omega}\left(\frac{1}{L_1} + \frac{1}{L_2}\right)\right]\sigma_0 \begin{bmatrix} V_{d\uparrow}^{m,n} \\ V_{d\downarrow}^{m,n} \end{bmatrix} \\
&\quad - \frac{1}{\mathrm{i}\omega L_1}\sigma_x \begin{bmatrix} V_{b\uparrow}^{m,n} \\ V_{b\downarrow}^{m,n} \end{bmatrix} - \frac{1}{\mathrm{i}\omega L_1}\sigma_y \begin{bmatrix} V_{a\uparrow}^{m,n} \\ V_{a\downarrow}^{m,n} \end{bmatrix} \\
&\quad - \frac{1}{\mathrm{i}\omega L_2}\sigma_x \begin{bmatrix} V_{b\uparrow}^{m-1,n} \\ V_{b\downarrow}^{m-1,n} \end{bmatrix} - \frac{1}{\mathrm{i}\omega L_2}\sigma_y \begin{bmatrix} V_{a\uparrow}^{m,n-1} \\ V_{a\downarrow}^{m,n-1} \end{bmatrix}. \qquad \text{(B5)}
\end{aligned}$$

The Laplacian matrix $J(\omega)$ of the circuit network is then given by

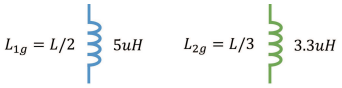
$$J(\omega) = \sum_{m,n}\Big(J_a(\omega) a_{m,n}^\dagger a_{m,n} + J_b(\omega) b_{m,n}^\dagger b_{m,n}$$

$$
\begin{aligned}
&+J_c(\omega)c^{\dagger}_{m,n}c_{m,n}+J_d(\omega)d^{\dagger}_{m,n}d_{m,n}\Big)\\
&+\sum_{m,n}\Big(-\frac{1}{\mathrm{i}\omega L_1}\sigma_x a^{\dagger}_{m,n}c_{m,n}-\frac{1}{\mathrm{i}\omega L_1}\sigma_x b^{\dagger}_{m,n}d_{m,n}\\
&-\frac{1}{\mathrm{i}\omega L_1}\sigma_y a^{\dagger}_{m,n}d_{m,n}-\frac{1}{\mathrm{i}\omega L_1}\sigma_y b^{\dagger}_{m,n}c_{m,n}\\
&-\frac{1}{\mathrm{i}\omega L_2}\sigma_x a^{\dagger}_{m,n}c_{m-1,n}-\frac{1}{\mathrm{i}\omega L_2}\sigma_x d^{\dagger}_{m,n}b_{m-1,n}\\
&-\frac{1}{\mathrm{i}\omega L_2}\sigma_y a^{\dagger}_{m,n}d_{m,n-1}\\
&-\frac{1}{\mathrm{i}\omega L_2}\sigma_y c^{\dagger}_{m,n}b_{m,n-1}+\mathrm{h.c.}\Big). \qquad \text{(B6)}
\end{aligned}
$$

Here, $J_i(\omega)$ denotes the on-site contribution of the circuit Laplacian associated with site i ($i=a,b,c,d$). At the circuit resonant frequency ω_0, the diagonal elements of $J(\omega_0)$ are effectively nullified through a carefully designed grounding scheme. Consequently, the resulting Laplacian matrix $J(\omega_0)$ establishes a direct correspondence with the Hamiltonian of the theoretical 2D SOC SOTI model, enabling a faithful experimental realization of its topological properties.

Appendix C: Circuit network grounding setup

In Appendix B, we provide detailed descriptions of the circuit network implementations for both the 1D SOC AB cage model and the 2D SOC SOTI model. In each case, we faithfully reproduce the theoretical Hamiltonians through carefully designed grounding schemes. For the 1D SOC AB cage, the specific grounding configuration is illustrated in Fig. C1, ensuring that each unit cell resonates at the target frequency and that the circuit precisely mimics the SOC-induced hopping terms. In the 2D SOC SOTI circuit, a distinct grounding strategy is employed, with individual nodes grounded differently to ensure a uniform resonant frequency ω_0 across the network. This approach allows the circuit to faithfully realize the higher-order topological features predicted by theory. The complete grounding settings for all nodes in the 2D circuit are summarized in Fig. C2.



i \ n	1	2	3	4	5	6
B						
A						
C						

Fig. C1. The grounding configuration of the circuit network for the 1D SOC AB cage model.

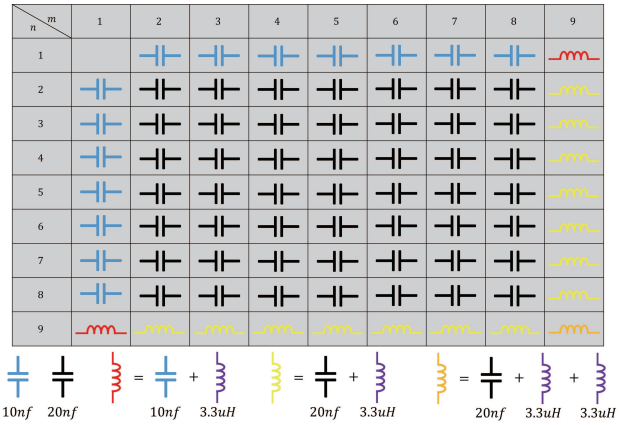


Fig. C2. The grounding configuration of the circuit network for the 2D SOC SOTI model.

Appendix D: Experimental measurement

We outline the experimental protocols for the circuit measurements presented in this work, focusing first on the 1D non-Abelian lattice. As illustrated in Fig. D1, the impedance spectroscopy setup provides electrical access to each lattice site via BNC connectors mounted on the PCB, ensuring stable signal injection and reliable connections to external instrumentation (see Fig. D1(c)). To probe the spin-up subspace $|\uparrow\rangle$, we employed a phase-coherent excitation scheme using four AC voltage sources with relative phases $(0, 3\pi/2, \pi, \pi/2)$ and a fixed amplitude of 2.5 V. The excitation signals were generated by two two-channel digital signal generators (Rigol-DG2102) synchronized via an additional master generator (Rigol-DG1022U), as shown in Fig. D1(a). The AC frequency was swept from 0 to 3 MHz, covering all relevant resonant modes of the system. The impedance response was measured using a voltage-divider configuration with $R_0 = 430\ \Omega$. The circuit impedance Z_{circuit} was calculated as $Z_{\text{circuit}} = \frac{U_1 R_0}{U-U_1}$, where $U = 2.5$ V is the source voltage and U_1 is the voltage measured between the target node and ground. All voltage signals were acquired using a digital oscilloscope (Rigol-DS2202A), as shown in Fig. D1(b). The measurement

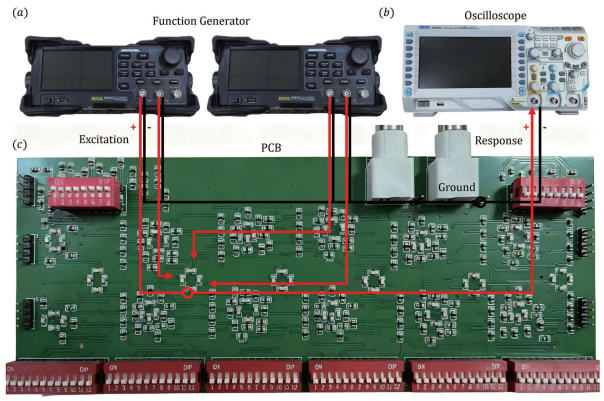


Fig. D1. Experimental setup and measurement circuit. (a) Photograph of the function generators used to provide phase-coherent AC excitations. (b) Photograph of the oscilloscope used for voltage measurements. (c) Photograph of the experimental PCB and the measurement-node connections.

protocol for the circuit implementation of the SOC SOTI follows the same procedure as that for the 1D lattice. The only difference is that the AC excitation frequency is swept from 0 to 2 MHz, while all other experimental settings and data acquisition procedures remain unchanged.

Appendix E: Topological phase diagram of the two-dimensional SOC higher-order model

To identify the parameter regime in which the higher-order topological phase persists in the two-dimensional SOC model, we compute the corresponding topological phase diagram as a function of the coupling ratio t_2/t_1, as shown in Fig. E1. For $0 < t_2/t_1 < 1$, the topological invariant remains $N = 0$, indicating that the system is in a topologically trivial phase and does not support higher-order boundary modes under open boundary conditions. As the coupling ratio crosses the critical point $t_2/t_1 = 1$, the topological invariant undergoes a quantized transition to $N = 2$, signaling the emergence of a nontrivial second-order topological phase. In this regime, two degenerate zero-energy corner modes appear at each corner of the lattice.

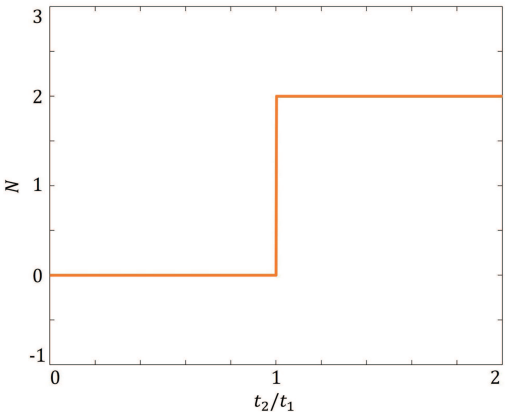


Fig. E1. Phase diagram of the two-dimensional SOC-induced higher-order topological model, characterized by the topological invariant N as a function of the hopping ratio t_2/t_1. The system is in the trivial phase with $N = 0$ for $0 < t_2/t_1 < 1$ and undergoes a topological transition at $t_2/t_1 = 1$, entering the higher-order topological phase with $N = 2$ for $t_2/t_1 > 1$.

Appendix F: Circuit simulation of the two-dimensional SOC higher-order model in the trivial phase

When the model parameters are in the trivial phase, the open-boundary energy spectrum exhibits a fully opened bulk gap, with no topological in-gap states such as corner or edge modes. In this section, we present the corresponding circuit simulation results for the two-dimensional SOC higher-order model, which illustrate this behavior. As shown in Fig. F1(a), the theoretically calculated admittance spectrum j_n of the circuit Laplacian features a pronounced gap at the resonant frequency f_0, with no spectral lines within the gap. Correspondingly, Fig. F1(b) shows the simulated grounding impedance spectra for corner, hinge, and bulk sites. The spectra are obtained by applying spin-up excitation and sweeping the driving frequency from 0 to 2 MHz. At the resonant frequency f_0, the grounding impedances at all sites are nearly zero, indicating that no response is observed and therefore no eigenmodes exist within the gap. These observations provide a clear contrast to the nontrivial phase discussed in the main text, further confirming the topological origin of the experimentally observed corner-state resonances.

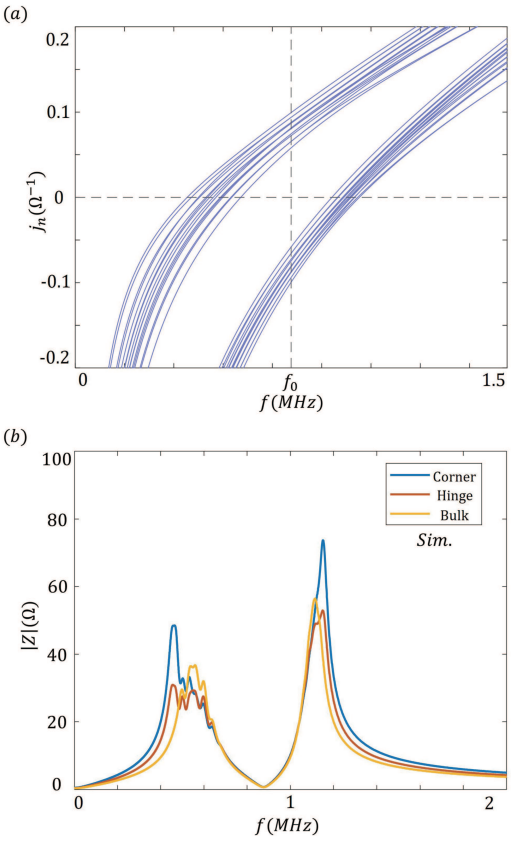


Fig. F1. (a) Theoretical admittance spectrum j_n of the circuit Laplacian under open boundary conditions, showing a clear bulk gap around the resonant frequency f_0 with no in-gap states. (b) Simulated grounding impedance spectra at a corner site, an edge site, and a bulk site under spin-up excitation. No pronounced impedance response is observed at any of the three sites near the resonant frequency f_0, indicating the absence of eigenstates within the gap. The circuit components are chosen as $C_1 = 10$ nF, $L_1 = 3.3$ μH, and $L_2 = 10$ μH, yielding a resonant frequency of $f_0 = 1/(2\pi\sqrt{C_1 L_1}) \approx 876$ kHz.

Appendix G: Robustness of SOC-induced topological states against disorders

In this section, we investigate the robustness of SOC-induced topological states against imperfections in circuit components. To this end, random perturbations are introduced into the circuit models, and the impedance responses of both the one-dimensional and two-dimensional systems are systematically analyzed. In the simulations, all circuit components — including inductors, capacitors, and parasitic resistances — are subjected to random perturbations of 10%, thereby mimicking unavoidable component tolerances in experiments.

For the one-dimensional SOC AB cage model, as shown in Fig. G1(a), the boundary-localized topological states still exhibit pronounced impedance enhancement at specific frequencies, while the dark and bulk states remain clearly distinguishable, despite moderate shifts in resonant frequencies and peak shapes caused by the perturbations. Similarly, for the two-dimensional SOC higher-order model, as shown in Fig. G1(b), the corner-site impedance remains significantly larger than those at edge and bulk sites near the resonant frequency f_0, forming a well-isolated resonant peak between the bulk and edge bands. This indicates that the higher-order topological corner states retain clear spectral separation and strong spatial localization under the same perturbation conditions.

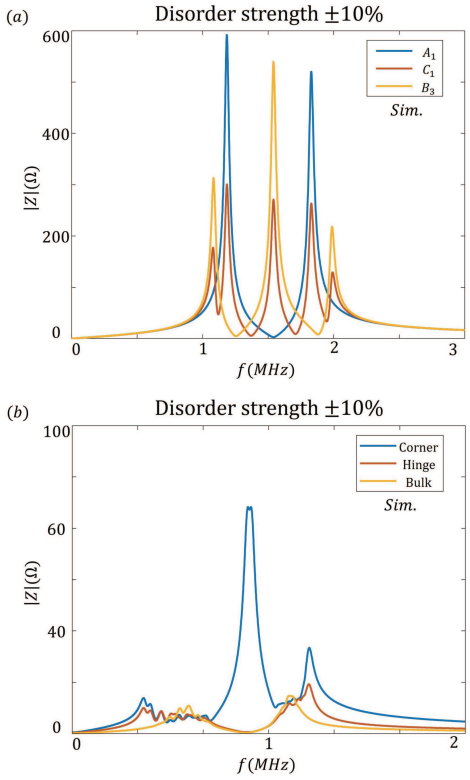


Fig. G1. (a) Simulated grounding impedance spectra of the one-dimensional SOC AB cage model in the topological phase, measured at sites A_1, C_1, and B_3 under 10% random perturbations of all circuit components. (b) Simulated grounding impedance spectra of the two-dimensional SOC higher-order model in the topological phase, measured at corner, edge, and bulk sites under the same 10% random perturbations.

Taken together, these results demonstrate that, even in the presence of 10% random component variations, the resonant peaks associated with SOC-induced topological boundary and corner states remain clearly distinguishable, confirming that these states are robust and protected by the underlying topology of the system.

Acknowledgments

This work was supported by the National Key Research and Development Program of China (Grant No. 2022YFA1404201), the National Natural Science Foundation of China (NSFC) (Grant Nos. 12474361, 12034012, 12074234), the Changjiang Scholars and Innovative Research Team in University of the Ministry of Education of China (PCSIRT) (*IRT*_17*R*70), the Fund for Shanxi 1331 Project Key Subjects Construction, the 111 Project (Grant No. D18001), and the Fundamental Research Program of Shanxi Province (Grant No. 202303021223005).

References

[1] Hasan M Z and Kane C L 2010 *Rev. Mod. Phys.* **82** 3045
[2] Qi X L and Zhang S C 2011 *Rev. Mod. Phys.* **83** 1057
[3] Bansil A, Lin H and Das T 2016 *Rev. Mod. Phys.* **88** 021004
[4] Asbóth J K, Oroszlány L and Pályi A 2016 *A Short Course on Topological Insulators* vol. 919 (Springer)
[5] Bernevig B A 2013 *Topological Insulators and Topological Superconductors* (Princeton University Press) pp. 45–98
[6] Rechtsman M C, Zeuner J M, Plotnik Y, Lumer Y, Podolsky D, Dreisow F, Nolte S, Segev M and Szameit A 2013 *Nature* **496** 196
[7] Lu L, Joannopoulos J D and Soljačić M 2014 *Nat. Photonics* **8** 821
[8] Wu Y, Li C, Hu X, Ao Y, Zhao Y and Gong Q 2017 *Adv. Opt. Mater.* **5** 1700357
[9] Khanikaev A B and Shvets G 2017 *Nat. Photonics* **11** 763
[10] Xie B Y, Wang H F, Zhu X Y, Lu M H, Wang Z and Chen Y F 2018 *Opt. Express* **26** 24531
[11] Ozawa T, Price H M, Amo A, Goldman N, Hafezi M, Lu L, Rechtsman M C, Schuster D, Simon J, Zilberberg O, *et al.* 2019 *Rev. Mod. Phys.* **91** 015006
[12] Kim M, Jacob Z and Rho J 2020 *Light Sci. Appl.* **9** 130
[13] Zhang D W, Tang L Z, Lang L J, Yan H and Zhu S L 2020 *Sci. China Phys. Mech. Astron.* **63** 267062
[14] Yan Q, Hu X, Fu Y, Lu C, Fan C, Liu Q, Feng X, Sun Q and Gong Q 2021 *Adv. Opt. Mater.* **9** 2001739
[15] Lan Z, Chen M L, Gao F, Zhang S and Sha W E 2022 *Rep. Phys.* **9** 100076
[16] Wang H X and Jiang J H 2022 *Front. Phys.* **10** 866552
[17] Hu X, Ma G, Lu C and Fu Y 2022 *Front. Phys.* **10** 953407
[18] Kang M, Liu T, Chan C T and Xiao M 2023 *Nat. Rev. Phys.* **5** 659
[19] Lu J, Deng W, Huang X, Ke M and Liu Z 2025 *Adv. Mater.* **37** 2307998
[20] Ma G, Xiao M and Chan C T 2019 *Nat. Rev. Phys.* **1** 281
[21] Zangeneh-Nejad F, Al'u A and Fleury R 2020 *C. R. Phys.* **21** 467
[22] Xue H, Yang Y and Zhang B 2022 *Nat. Rev. Mater.* **7** 974
[23] Lin Z K, Wang Q, Liu Y, Xue H, Zhang B, Chong Y and Jiang J H 2023 *Nat. Rev. Phys.* **5** 483
[24] Zhang X, Zangeneh-Nejad F, Chen Z G, Lu M H and Christensen J 2023 *Nature* **618** 687
[25] Ni X, Yves S, Krasnok A and Alu A 2023 *Chem. Rev.* **123** 7585
[26] Zhu W, Deng W, Liu Y, Lu J, Wang H X, Lin Z K, Huang X, Jiang J H and Liu Z 2023 *Rep. Prog. Phys.* **86** 106501
[27] Goldman N, Budich J C and Zoller P 2016 *Nat. Phys.* **12** 639
[28] Zhang D W, Zhu Y Q, Zhao Y, Yan H and Zhu S L 2018 *Adv. Phys.* **67** 253
[29] Cooper N, Dalibard J and Spielman I 2019 *Rev. Mod. Phys.* **91** 015005
[30] Lee C H, Imhof S, Berger C, Bayer F, Brehm J, Molenkamp L W, Kiessling T and Thomale R 2018 *Commun. Phys.* **1** 39
[31] Dong J, Juričić V and Roy B 2021 *Phys. Rev. Res.* **3** 023056
[32] Yang H, Song L, Cao Y and Yan P 2024 *Phys. Rep.* **1093** 1
[33] Chen T, Zhang W, Zou D, Sun Y and Zhang X 2025 *Adv. Quantum Technol.* **8** 2400448
[34] Sahin H, Jalil M B A and Lee C H 2025 *APL Electron. Devices* **1** 021503
[35] Wang P J, Yu Z Q, Fu Z K, Miao J, Huang L H, Chai S J, Zhai H and Zhang J 2012 *Phys. Rev. Lett.* **109** 095301
[36] Zhang J Y, Ji S C, Chen Z, Zhang L, Du Z D, Yan B, Pan G S, Zhao B, Deng Y J, Zhai H, *et al.* 2012 *Phys. Rev. Lett.* **109** 115301

[37] Huang L, Meng Z, Wang P, Peng P, Zhang S L, Chen L and Li D 2016 *Nat. Phys.* **12** 540
[38] Wu Z, Zhang L, Sun W, Xu X T, Wang B Z, Ji S C, Deng Y, Chen S, Liu X J and Pan J W 2016 *Science* **354** 83
[39] Wang Z Y, Cheng X C, Wang B Z, Zhang J Y, Lu Y H, Yi C R, Niu S, Deng Y, Liu X J, Chen S, *et al*. 2021 *Science* **372** 271
[40] Zhu S L, Fu H, Wu C J, Zhang S C and Duan L M 2006 *Phys. Rev. Lett.* **97** 240401
[41] Shao L, Zhu S L, Sheng L, Xing D and Wang Z 2008 *Phys. Rev. Lett.* **101** 246810
[42] Liu X J, Borunda M F, Liu X and Sinova J 2009 *Phys. Rev. Lett.* **102** 046402
[43] Liu X J, Liu Z X and Cheng M 2013 *Phys. Rev. Lett.* **110** 076401
[44] Liu X J, Law K T and Ng T K 2014 *Phys. Rev. Lett.* **112** 086401
[45] Zhang D W, Wang Z D and Zhu S L 2012 *Front. Phys.* **7** 31
[46] Cheng D, Wang K, Roques-Carmes C, Lustig E, Long O Y, Wang H and Fan S 2025 *Nature* **637** 52
[47] Wu J, Wang Z, Biao Y, Fei F, Zhang S, Yin Z, Hu Y, Song Z, Wu T, Song F, *et al*. 2022 *Nat. Electron.* **5** 635
[48] Zhai L X, Wang Y and Liu J J 2010 *Phys. Lett. A* **374** 4548
[49] Gou W, Chen T, Xie D, Xiao T, Deng T S, Gadway B, Yi W and Yan B 2020 *Phys. Rev. Lett.* **124** 070402
[50] Wang H, Zhang W, Sun H and Zhang X 2022 *Phys. Rev. B* **106** 104203
[51] Zhang W, Wang H, Sun H and Zhang X 2023 *Phys. Rev. Lett.* **130** 206401
[52] Li S, Xue Z Y, Gong M and Hu Y 2020 *Phys. Rev. A* **102** 023524
[53] Sugawa S, Salces-Carcoba F, Yue Y, Putra A and Spielman I 2021 *npj Quantum Inf.* **7** 144
[54] Yu R, Qi X L, Bernevig A, Fang Z and Dai X 2011 *Phys. Rev. B* **84** 075119
[55] Zhu S L 2006 *Phys. Rev. Lett.* **96** 077206
[56] Kremer M, Petrides I, Meyer E, Heinrich M, Zilberberg O and Szameit A 2020 *Nat. Commun.* **11** 907
[57] Benalcazar W A, Bernevig B A and Hughes T L 2017 *Science* **357** 61
[58] Imhof S, Berger C, Bayer F, Brehm J, Molenkamp L W, Kiessling T, Schindler F, Lee C H, Greiter M, Neupert T, *et al*. 2018 *Nat. Phys.* **14** 925
[59] Noh J, Benalcazar W A, Huang S, Collins M J, Chen K P, Hughes T L and Rechtsman M C 2018 *Nat. Photonics* **12** 408
[60] Peterson C W, Benalcazar W A, Hughes T L and Bahl G 2018 *Nature* **555** 346
[61] Serra-Garcia M, Peri V, Süsstrunk R, Bilal O R, Larsen T, Villanueva L G and Huber S D 2018 *Nature* **555** 342
[62] Xie B Y, Wang H F, Wang H X, Zhu X Y, Jiang J H, Lu M H and Chen Y F 2018 *Phys. Rev. B* **98** 205147
[63] El Hassan A, Kunst F K, Moritz A, Andler G, Bergholtz E J and Bourennane M 2019 *Nat. Photonics* **13** 697
[64] Mittal S, Orre V V, Zhu G, Gorlach M A, Poddubny A and Hafezi M 2019 *Nat. Photonics* **13** 692
[65] Xie B Y, Su G X, Wang H F, Su H, Shen X P, Zhan P, Lu M H, Wang Z L and Chen Y F 2019 *Phys. Rev. Lett.* **122** 233903
[66] Zhang X, Xie B Y, Wang H F, Xu X, Tian Y, Jiang J H, Lu M H and Chen Y F 2019 *Nat. Commun.* **10** 5331
[67] Zhang X, Wang H X, Lin Z K, Tian Y, Xie B Y, Lu M H, Chen Y F and Jiang J H 2019 *Nat. Phys.* **15** 582
[68] Ni X, Weiner M, Alu A and Khanikaev A B 2019 *Nat. Mater.* **18** 113
[69] Xue H, Yang Y, Gao F, Chong Y and Zhang B 2019 *Nat. Mater.* **18** 108
[70] Ni X, Li M, Weiner M, Al'u A and Khanikaev A B 2020 *Nat. Commun.* **11** 2108
[71] Qi Y, Qiu C, Xiao M, He H, Ke M and Liu Z 2020 *Phys. Rev. Lett.* **124** 206601
[72] Wang H X, Lin Z K, Jiang B, Guo G Y and Jiang J H 2020 *Phys. Rev. Lett.* **125** 146401
[73] Ghorashi S A A, Li T and Hughes T L 2020 *Phys. Rev. Lett.* **125** 266804
[74] Luo L, Wang H X, Lin Z K, Jiang B, Wu Y, Li F and Jiang J H 2021 *Nat. Mater.* **20** 794
[75] Wang B Q, Wu H and An J H 2021 *Phys. Rev. B* **104** 205117
[76] Wei Q, Zhang X, Deng W, Lu J, Huang X, Yan M, Chen G, Liu Z and Jia S 2021 *Nat. Mater.* **20** 812
[77] Wu H, Wang B Q and An J H 2021 *Phys. Rev. B* **103** L041115
[78] Yang Y, Lu J, Yan M, Huang X, Deng W and Liu Z 2021 *Phys. Rev. Lett.* **126** 156801
[79] Qiu H, Xiao M, Zhang F and Qiu C 2021 *Phys. Rev. Lett.* **127** 146601
[80] Wang Y, Xie B Y, Lu Y H, Chang Y J, Wang H F, Gao J, Jiao Z Q, Feng Z, Xu X Y, Mei F, *et al*. 2021 *Light Sci. Appl.* **10** 173
[81] Du J, Li T, Fan X, Zhang Q and Qiu C 2022 *Phys. Rev. Lett.* **128** 224301
[82] Huang X, Lu J, Yan Z, Yan M, Deng W, Chen G and Liu Z 2022 *Sci. Bull.* **67** 488
[83] Schulz J, Noh J, Benalcazar W A, Bahl G and von Freymann G 2022 *Nat. Commun.* **13** 6597
[84] Wu S Q, Lin Z K, Jiang B, Zhou X, Hang Z H, Hou B and Jiang J H 2022 *Phys. Rev. Appl.* **17** 034061
[85] Yamada S S, Li T, Lin M, Peterson C W, Hughes T L and Bahl G 2022 *Nat. Commun.* **13** 2035
[86] Gao M J, Wu H and An J H 2023 *Phys. Rev. B* **107** 035128
[87] Gao M J, Wu H and An J H 2023 *Phys. Rev. B* **108** L241402
[88] Li Y, Qiu H, Zhang Q and Qiu C 2023 *Phys. Rev. B* **108** 205135
[89] Li Y, Zhang J H, Mei F, Xie B Y, Lu M H, Ma J, Xiao L and Jia S 2023 *Phys. Rev. Appl.* **20** 064042
[90] Xia T, Li Y, Zhang Q, Fan X, Xiao M and Qiu C 2023 *Phys. Rev. B* **108** 125125
[91] Jia W, Wang B Z, Gao M J and An J H 2024 *Phys. Rev. B* **110** L201117
[92] Koh J M, Tai T and Lee C H 2024 *Nat. Commun.* **15** 5807
[93] Ma Q, Pu Z, Ye L, Lu J, Huang X, Ke M, He H, Deng W and Liu Z 2024 *Phys. Rev. Lett.* **132** 066601
[94] Qiu H, Li Y, Zhang Q and Qiu C 2024 *Phys. Rev. Lett.* **132** 186601
[95] Shang C, Liu S, Jiang C, Shao R, Zang X, Lee C H, Thomale R, Manchon A, Cui T J and Schwingenschlögl U 2024 *Adv. Sci.* **11** 2303222
[96] Zhang J H, Mei F, Xiao L and Jia S 2024 *Phys. Rev. Lett.* **132** 036603
[97] Wang Q and Hao N 2024 *Chin. Phys. B* **33** 127303
[98] Hua C and Xu D H 2025 *Chin. Phys. B* **34** 037301
[99] Lü S and Hu J 2025 *Chin. Phys. B* **34** 117303
[100] Zhang J H, Mei F, Li Y, Lee C H, Ma J, Xiao L and Jia S 2025 *Nat. Commun.* **16** 2050
[101] Qian H, Gong M, Zhang J, Guo S, Zha C, Chen F, Ye Y, Wu Y, Cao S, Ying C, *et al*. 2025 *Science* **390** 930
[102] Benalcazar W A and Cerjan A 2022 *Phys. Rev. Lett.* **128** 127601
[103] Nagulu A, Ni X, Kord A, Tymchenko M, Garikapati S, Al'u A and Krishnaswamy H 2022 *Nat. Electron.* **5** 300
[104] Yuan H, Zhang W, Zhou Z, Wang W, Pan N, Feng Y, Sun H and Zhang X 2023 *Adv. Sci.* **10** 2301128
[105] Zhou X, Zhang W, Cao W and Zhang X 2025 *Phys. Rev. Lett.* **135** 106601